This article has been accepted for inclusion in a future issue of this journal. Content is final as presented, with the exception of pagination.

Spatially Distributed MIMO Sonar Systems: Principles and Capabilities

Yan Pailhas, Yvan Petillot, *Member, IEEE*, Keith Brown, and Bernard Mulgrew, *Fellow, IEEE*

***Abstract*—Multiple-input–multiple-output (MIMO) sonar systems offer new perspectives for target detection and area surveillance. This paper introduces a unified formulation for sonar MIMO systems and focuses on the target detection and recognition capability of these systems. The multiplication of the number of transmitters and receivers not only provides a greater variety in terms of target view angles but also provides meaningful statistics on the target itself. Assuming that views are independent and the MIMO system is large enough, we demonstrate that target recognition is possible with only one MIMO snapshot. By studying the detection performance of MIMO sonars we also demonstrate that such systems solve the speckle noise and decorrelate individual scatterers inside one cell resolution, leading to super-resolution imaging. We also show that, if carefully designed, MIMO systems can surpass the resolution of a synthetic aperture sonar (SAS) system using the same bandwidth. All the discussed properties are derived from the independent view assumption. Fulfilling this assumption drives the design and efficiency of such systems.**

***Index Terms*—MIMO sonar systems, multistatic sonars, target recognition, super-resolution sonar images.**

I. Introduction

MULTIPLE-INPUT–MULTIPLE-OUTPUT (MIMO) does not have a strict and formal definition [1]. In this paper, we define MIMO as a structure with multiple transmitters and receivers which transmits a variety of waveforms and has the capability to jointly process all the received signals. MIMO systems can have collocated [2] or widely separated [3] antennas. This paper focuses on spatially distributed MIMO structures. MIMO has been widely investigated during the last two decades for wireless communications, and has received a lot of interest in recent years in the radar community [4]–[8]. Radar researchers have pointed out multiple advantages of these systems such as diversity gain for target detection [2], [6], [9], [10], angle of arrival [11], [12], and Doppler estimation [3], [13]. Coherent processing also allows improved resolution for target localization [14].

Multistatic sonar systems have also been investigated, mainly in the antisubmarine warfare community. Such systems surpass monostatic sonar systems in target localization [15] and detection performance [16]. The Centre for Maritime Research and Experimentation (CMRE, la Spezia, Italy), in particular, has developed a deployable low-frequency multistatic sonar system called DEMUS. The DEMUS hardware consists of one source and three receiver buoys and can be denominated as a single-input–multiple-output (SIMO) system. A series of trials including preDEMUS06 and SEABAR07 [17], [18] have been conducted by CMRE. Results of these trials show better detection and tracking performances [17]–[22]. However, very few studies have investigated full MIMO sonar systems.

This paper focuses on the detection and recognition problems using MIMO sonar systems with widely separated antennas. The main contributions of the paper are as follows.

1) The reformulation of the MIMO equations for sonar systems (Section II). The model proposed is based on the target form function formulation and, unlike the radar formulation, intelligibly dissociates propagation from target response. Although the model is derived from the radar formulation, this approach emphasizes the fundamental differences between radar and sonar systems.
2) A new bistatic modeling of cylindrical shell using virtual point scatterers (Section III). The echo of man-made objects with a relatively simple shape can be modeled with very few scattering points. We show in Section III an example of this statement.
3) The derivation of the recognition capability of MIMO sonar systems (Section IV-A). Studying the target response from a MIMO system leads to the observation that, with enough independent observations, the target probability density function is very well estimated with a single snapshot. An example of automatic target recognition is presented.
4) The proof that MIMO systems can resolve the speckle (Section IV-B). By fusing the target response of a well-designed MIMO system, we demonstrate that when the number of independent observations is close to infinity, all the scatterers within one resolution cell decorrelate.

It is important to note that results 3) and 4) on the MIMO sonar capabilities are derived independently of any particular MIMO system geometry. The assumption of independent observations between all the MIMO pairs is discussed (Section IV-C). A novel measure of intercorrelation for a MIMO sonar system based on the distance correlation [23] is proposed to measure effectively the degree of independence of all the MIMO observations.

This paper is organized as follows. In Section II, we present the radar MIMO formulation and derive the broadband sonar MIMO expression. Section II-A focuses on the MIMO

Manuscript received February 27, 2015; revised September 16, 2015, February 17, 2016, June 8, 2016, and July 12, 2016; accepted July 14, 2016. This work was supported by the Engineering and Physical Sciences Research Council (EPSRC) under Grant EP/J015180/1 and the MOD University Defence Research Collaboration in Signal Processing under Grant EP/K014277/1.

Associate Editor: T. Sæbø.

Y. Pailhas, Y. Petillot, and K. Brown are with the Ocean Systems Laboratory, Heriot Watt University, Edinburgh EH14 4AS, U.K. (e-mail: Y.Pailhas@hw.ac.uk; Y.R.Petillot@hw.ac.uk; K.E.Brown@hw.ac.uk).

B. Mulgrew is with the School of Engineering, Edinburgh University, Edinburgh EH9 3JL, U.K. (e-mail: bernie@staffmail.ed.ac.uk).

Digital Object Identifier 10.1109/JOE.2016.2593602

response of targets modeled by a finite point scatterers model. In Section III, a finite point scatterer model for a bistatic system is presented for a resonant target. Finally, in Section IV, we demonstrate the sonar MIMO capabilities in terms of target recognition and MIMO very-high-resolution imaging.

II. Reformulation of the Broadband MIMO Sonar Problem

A. The RADAR Formulation

The first formulation for MIMO systems for target detection has been made by the radar community [4]. The MIMO system model can usually be expressed by $\overline{\mathbf{r}} = \overline{\overline{\mathbf{H}}}.\overline{\mathbf{s}} + \overline{\mathbf{n}}$, where $\overline{\mathbf{r}}$ represents the receivers, $\overline{\mathbf{s}}$ represents the transmitters, $\overline{\mathbf{n}}$ is noise, and $\overline{\overline{\mathbf{H}}}$ is the channel matrix. The channel matrix includes the wave propagation in the medium from any transmitter to any receiver and the target reflections. Some models use the point target assumption [24] while more advanced versions use rectangular-shape targets composed of an infinite number of scatterers [6]. We present here the most popular model for a radar target which is the finite scatterer model [3], [10].

In [3], Haimovich *et al.* formulate the narrowband MIMO radar equation using a finite point target model. A target is represented here with Q scattering points spatially distributed. Let $\{X_q\}_{q\in[1,Q]}$ be their locations. The reflectivity of each scattering point is represented by the complex random variable ζ_q. All the ζ_q are assumed to be zero-mean, independent and identically distributed with a variance $\mathbb{E}[|\zeta_q|^2] = 1/Q$. Let Σ be the reflectivity matrix of the target $\Sigma = \mathrm{diag}(\zeta_1, \dots, \zeta_Q)$. By using this notation, the average radar cross section (RCS) of the target $\{X_q\}$, $\mathbb{E}[\Sigma\Sigma^T]$, is normalized to 1.

The MIMO system comprises a set of K transmitters and L receivers. Each transmitter k sends the pulse $\sqrt{E/K}.s_k(t)$ where E is the total transmit energy of the MIMO system. We assume that all the pulses $s_k(t)$ are normalized. With these notations, the signal $z_{lk}(t)$ from transmitter t to receiver l and interacting with the target can be written as

$$z_{lk}(t) = \sqrt{\frac{E}{K}} \sum_{q=1}^{Q} h_{lk}^{(q)} s_k\left(t - \tau_{tk}(X_q) - \tau_{rl}(X_q)\right) \quad (1)$$

with

$$h_{lk}^{(q)} = \zeta_q \mathrm{e}^{-j2\pi f_c[\tau_{tk}(X_q)+\tau_{rl}(X_q)]} \quad (2)$$

where f_c is carrier frequency, $\tau_{tk}(X_q)$ represents the propagation time delay between the transmitter k and the scattering point X_q, and $\tau_{rl}(X_q)$ represents the propagation time delay between the scattering point X_q and the receiver l. Note that $h_{lk}^{(q)}$ represents the total phase shift due to the propagation from the transmitter k to the scattering point X_q, the propagation from the scattering point X_q to the receiver l, and the reflection on the scattering point X_q.

Assuming that the Q scattering points are close together (i.e., within a resolution cell), we can write

$$\begin{aligned} s_k\left(t - \tau_{tk}(X_q) - \tau_{rl}(X_q)\right) &\approx s_k\left(t - \tau_{tk}(X_0) - \tau_{rl}(X_0)\right) \\ &= s_k^l(t, X_0) \end{aligned} \quad (3)$$

where X_0 is the center of gravity of the target $\{X_q\}$. So (1) becomes

$$\begin{aligned} z_{lk}(t) &= \sqrt{\frac{E}{K}} s_k^l(t, X_0) \left(\sum_{q=1}^{Q} \zeta_q \mathrm{e}^{-j2\pi f_c[\tau_{tk}(X_q)+\tau_{rl}(X_q)]}\right) && (4) \\ &= \sqrt{\frac{E}{K}} \left(\sum_{q=1}^{Q} h_{lk}^{(q)}\right) s_k^l(t, X_0) && (5) \\ &= \sqrt{\frac{E}{K}}\, h_{lk}\; s_k^l(t, X_0) && (6) \end{aligned}$$

using the notation $h_{lk} = \sum_{q=1}^{Q} h_{lk}^{(q)}$. Assuming a multitarget scenario including N_0 targets, the total signal $r_{lk}(t)$ from transmitter l to receiver k can be written as

$$r_{lk}(t) = \sum_{n=1}^{N_0} z_{lk}^{(n)}(t) + n_{lk}(t) \quad (7)$$

where n_{lk} is the total noise at receiver k. Note that the interaction between targets is ignored here.

In this section, we propose a reformulation of the Haimovich model presented in Section II-A to suit broadband sonar systems. Because the target response, the seabed, and surface response or even the wave propagation is strongly dependent of the frequency, a broadband sonar formulation is more appropriate in the Fourier domain [25]–[27]. It also allows a clear separation of the different mechanisms involved in the echo formation. Equation (1) becomes

$$Z_{lk}(\omega) = \sqrt{\frac{E}{K}} \sum_{q=1}^{Q} h_{lk}^{(q)} S_k(\omega) \mathbf{e}^{-j\omega[\tau_{tk}(X_q)+\tau_{rl}(X_q)]}. \quad (8)$$

Using the following notations:

$$\begin{aligned} \tau_{tk}(X_q) &= \tau_{tk}(X_0) + \tilde{\tau}_{tk}(X_q) \\ \tau_{rl}(X_q) &= \tau_{rl}(X_0) + \tilde{\tau}_{tk}(X_q) \end{aligned} \quad (9)$$

and

$$H_{lk}(X_0, \omega) = \sqrt{\frac{E}{K}}.\mathbf{e}^{-j(2\pi f_c+\omega).[\tau_{tk}(X_0)+\tau_{rl}(X_0)]} \quad (10)$$

the following expression can be derived:

$$\begin{aligned} Z_{lk}(\omega) &= H_{lk}(X_0, \omega) \left(\sum_{q=1}^{Q} \tilde{h}_{lk}^{(q)} \mathbf{e}^{-j\omega[\tilde{\tau}_{tk}(X_q)+\tilde{\tau}_{rl}(X_q)]}\right) S_k(\omega) \\ &= H_{lk}(X_0, \omega) F_\infty(\omega, \theta_l, \phi_k) S_k(\omega) \end{aligned} \quad (11)$$

where θ_l is the angle of view of the target from the transmitter and ϕ_k is the angle of view of the target from the receiver. Equation (11) can be interpreted as follows: the first term corresponds to the propagation of the wave to and from the target, the second term is the form function of the target, and the third term is the transmitted signal.

The main advantage of this formulation is the clear separation between propagation terms and target reflection terms. In our formulation, the target form function F_∞ is independent of any particular model. The second advantage of this formulation is that the generalization of (11) including multipath and

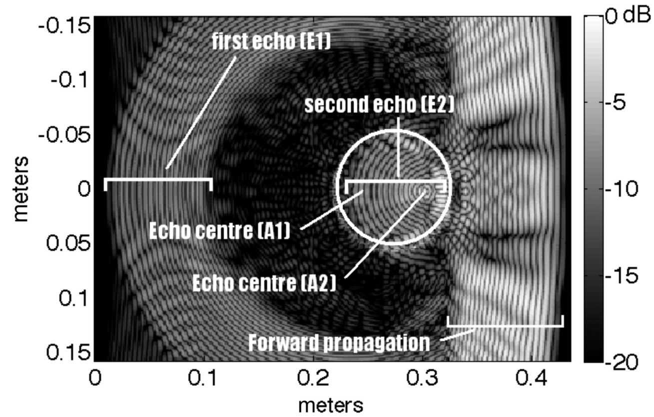

Fig. 1. Sound interaction between a plane wave and a plastic cylindrical shell.

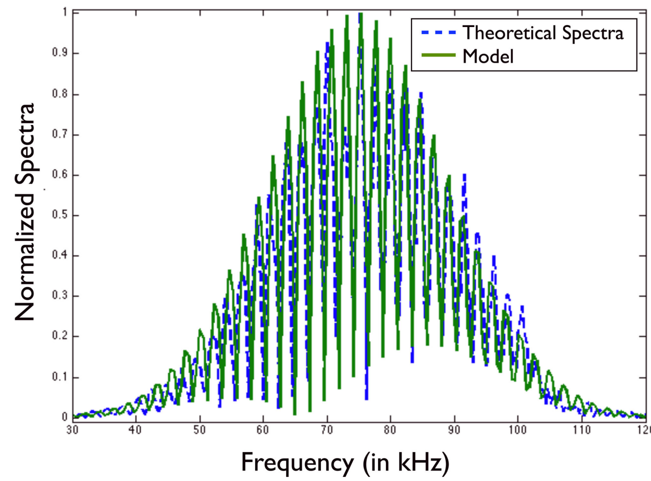

Fig. 2. Matching between the normalized spectra between the theoretical prediction [32] and our model.

attenuation terms is straightforward. Considering P multipaths between the transmitter l and the receiver k, (11) becomes

$$Z_{lk}(\omega) = \sum_{p=1}^{P} A^{(p)}(\omega) H_{lk}^{(p)}(X_0, \omega) F_\infty(\omega, \theta_l^{(p)}, \phi_k^{(p)}) S_k(\omega). \tag{12}$$

$A^{(p)}(\omega)$ is the attenuation through path p.

In this formulation, we choose to ignore the Doppler shift introduced by a moving target. Considering a target moving at $v = 1$ m.s^{-1} and a pulse with $f_0 = 50$ kHz central frequency, the maximum Doppler shift is $\delta f = 2 f_0 v / c \approx 67$ Hz. Narrowband Doppler-sensitive pulses have minimal spectral width. In that case, the spectral width is dominated by the pulse width. With a pulse duration of $\tau = 10^{-3}$ s, the maximal Doppler shift of 67 Hz is then marginal compared to the 2.5-kHz spectral width.

III. Virtual Point Scatterers Model for a Cylindrical Shell

We derived earlier the MIMO sonar model from the finite point scatterer model. In this section, we analyze further this target model. Despite the simplicity of this model, we demonstrated in [28]–[30] that for monostatic sonar systems, man-made objects can be reasonably well modeled using this approach. We even showed in [30] that this assumption leads to interesting features to distinguish man-made objects from natural objects. We extend here the monostatic point scatterer model to an accurate bistatic model for a low impedance shell cylinder.

In [29], we demonstrated that the sound scattering of a low impedance shell cylinder is analogous to the reflection by two spherical mirrors (one convex for the front face and one concave for the back face) in geometrical optics. Fig. 1 shows the echo formation of an acoustic wave reflected by a plastic cylindrical shell. The location of the two echo centers A1 and A2 (in Fig. 1) can be computed thanks to the well-known formula of reflection by a spherical mirror [31]

$$\frac{1}{\overline{\mathbf{SA}'}} + \frac{1}{\overline{\mathbf{SA}}} = \frac{2}{\overline{\mathbf{SC}}} \tag{13}$$

where $\mathbf{A}$ and $\mathbf{A}'$ represent, respectively, the source and the source image, $\mathbf{C}$ is the center of the sphere, and $\mathbf{SC}$ is the radius of the sphere.

A1 and A2 are the source images of an incoming plane wave. The two echo centers A1 and A2 are then exactly between the center of the cylinder and the front and the back of the cylinder. In our model, A1 and A2 will represent the virtual scatterers. They act like point sources, but contrary to scattering points, they emit the received pulse with a delay (positive or negative).

The transmitter k transmits the pulse $s_k(t)$. The acoustic wave is reflected by the cylinder modeled by the virtual scatterers A1 and A2 to receiver l. Equation (14) expresses the acoustic field $r_{kl}(t)$ received at receiver l

$$\begin{aligned} r_{kl}(t) = \; & s_k\left(t - \tau_{kC} - \frac{3}{2}\frac{SC}{c} - \tau_{A_1 l}\right) \mathbf{e}^{i\psi_1} \\ & + s_k\left(t - \tau_{kC} + \frac{3}{2}\frac{SC}{c} - \tau_{A_2 l}\right) \mathbf{e}^{i\psi_2} \end{aligned} \tag{14}$$

where SC represents the radius of the cylinder, c is the speed of sound in water, C is the center of the cylinder, and the notation τ_{kC} represents the propagation time between the transmitter k and C, and $\tau_{A_i l}$ represents the propagation time between the virtual scatterer Ai and the receiver l. ψ_i corresponds to the phase shift introduced by the virtual scatterer Ai. For this case, $\psi_1 = \psi_2 = 0$.

The two terms $-3/2(SC/c)$ and $+3/2(SC/c)$ represent the negative and positive delays of the virtual scatterers. In Fig. 2, we compare the echo spectra of our virtual scattering point model with the analytic solution given in [32]. In this example, the cylindrical shell is made of PVC, its diameter is 32 cm, and its thickness is 3 mm. The receiver is placed at 4 m from the shell at an angle of 30° relative to broadside. An excellent match is found between the theoretical prediction and our model.

This result as well as results from [28]–[30] reenforces our assumption that a simple shaped man-made target echo can be modeled with a finite and small number of scatterers. This

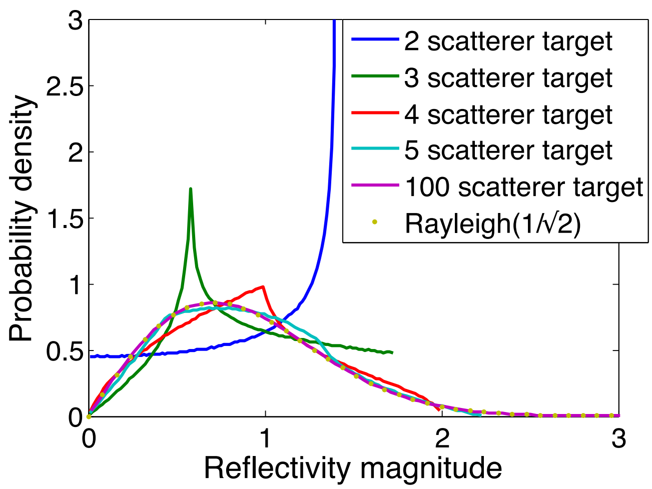

Fig. 3. Reflectivity probability density functions of a Q scattering point target with $Q = 2, 3, 4, 5$ & 100 using the scatterer reflectivity model from (15).

assumption differs greatly from radar models where targets are modeled with high-density scattering points.

IV. Statistical MIMO

A. Automatic Target Recognition Using Statistical MIMO

It is interesting to note that the term $\sum_{q=1}^{Q} h_{lk}^{(q)}$ in (5) corresponds in essence to a random walk in the complex plane where each step $h_{lk}^{(q)}$ can be modeled by a random variable. Random walks are often used in physics to model the particle diffusion in gas or liquid. Lets assume that the reflectivity coefficients ζ_q can be modeled by the random variable $\frac{1}{\sqrt{Q}}\mathrm{e}^{2i\pi U}$ where $U \in [0, 1]$ is the uniform distribution. This hypothesis implies that

$$h_{lk}^{(q)} = \frac{1}{\sqrt{Q}}\mathrm{e}^{2i\pi U}. \tag{15}$$

The independence of each $h_{lk}^{(q)}$ lies in the fact that the antennas are widely spaced and there is no correlation between each transmit $\longrightarrow$ scattering point $\longrightarrow$ receiver path. Using the central limit theorem, we can compute the limit

$$\lim_{Q\to+\infty} \sqrt{\left|\sum_{q=1}^{Q} h_{lk}^{(q)}\right|^2} \sim \mathrm{Rayleigh}(1/\sqrt{2}). \tag{16}$$

Rayleigh(σ) represents the Rayleigh-distributed random variable with parameter σ. Here $\sigma = 1/\sqrt{2}$. However, the central limit theorem gives only the asymptotic behavior of the random variable. As the number of scattering points becomes large, the reflectivity of the target can be modeled by a Rayleigh distribution.

Equation (16) links the expected reflectivity of the target $\{X_q\}$ to the expected diffusion of a particle following the random walk $\sum_{q=1}^{Q} h_{lk}^{(q)}$. It has been proven in [33] that the convergence of (16) is fast. To demonstrate this, we use the Moivre–Laplace representation [which compares probability density functions (pdfs)] to visualize the pdf convergence. In Fig. 3, we compute the pdf of the reflectivity of a Q scattering point target using the model given by (15). As this figure shows, for $Q \geq 5$, the reflectivity pdf matches closely the Rayleigh$(1/\sqrt{2})$ probability distribution. In Fig. 3, we can see that the probability function of the 100 scatterer target and Rayleigh$(1/\sqrt{2})$ are almost indistinguishable.

We also note in Fig. 3 that while the convergence of the reflectivity distribution function to a Rayleigh distribution is fast, the reflectivity of a target with few scattering points ($Q \in [2, 3, 4]$) presents a very characteristic pdf. The small number scatterer targets are particularly interesting because they are more likely to represent simple shaped man-made target (cf., Section III).

Monostatic sonar systems only provide one observation of the target per cycle. However, with MIMO systems, assuming widely separated antennas, we have access to $N = K \times L$ independent observations, where K is the total number of transmitters and L is the total number of receivers. The question we are asking here is: Can we estimate the number of scattering points of a target with a large MIMO system? If yes, how many observations (N) are needed to estimate the scattering point density?

Here we want to take advantage of the dissimilarities of the probability density functions to estimate the number of scattering points. Each observation is a realization of the random variable $\gamma_n = \sqrt{\left|\sum_{q=1}^{Q} h_{lk}^{(q)}\right|^2}$ with Q the number of scattering points. Each set of observations $\Gamma = \{\gamma_n\}_{n\in[1,N]}$ represents the MIMO output (N is the total number of observations). Given a set of observations Γ we can compute the probability that the target has Q scatterers using Bayes rules

$$\mathrm{P}(T_Q|\Gamma) = \frac{\mathrm{P}(\Gamma|T_Q)\mathrm{P}(T_Q)}{\mathrm{P}(\Gamma)} \tag{17}$$

where T_Q represents the event that the target has Q scatterers. Assuming the independence of the observations $\mathrm{P}(\Gamma|T_Q)$ can be written as

$$\mathrm{P}(\Gamma|T_Q) = \prod_{n=1}^{N} \mathrm{P}(\gamma_n|T_Q). \tag{18}$$

$\mathrm{P}(\gamma_n|T_Q)$ is computed with the aid of the reflectivity density function presented in Fig. 3. We consider four target types: two scatterer target, three scatterer target, four scatterer target, and five plus scatterer target. So $Q \in \{2, 3, 4, 5+\}$. Therefore, we can write

$$\mathrm{P}(\Gamma) = \sum_{Q=2}^{5} \mathrm{P}(\Gamma|T_Q)\mathrm{P}(T_Q). \tag{19}$$

Given that we have no *a priori* information about the target, we can assume that $\mathrm{P}(T_Q)$ is equal for all target class T_Q. Equation (17) then becomes

$$\mathrm{P}(T_Q|\Gamma) = \frac{\prod_{n=1}^{N} \mathrm{P}(\gamma_n|T_Q)}{\sum_{Q=2}^{5+} \mathrm{P}(\Gamma|T_Q)}. \tag{20}$$

The estimated target class corresponds to the class which maximizes the conditional probability given by (20).

To validate the theory, a number of experiments have been run in simulation. In the first experiment, 10^6 classification tests

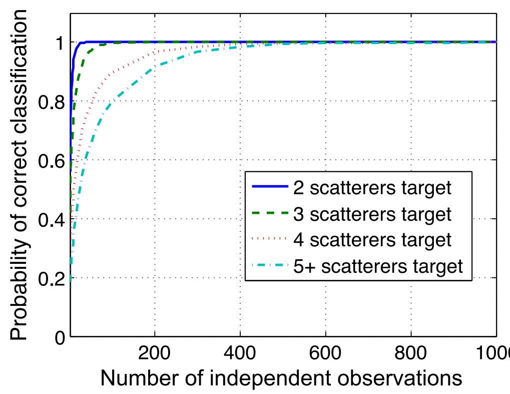

(a)

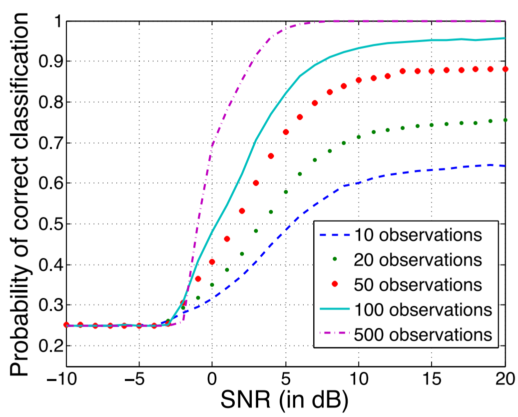

(b)

Fig. 4. (a) Correct classification probability against the number of independent observations for four classes of targets (two, three, four, and five plus scattering point targets). (b) Overall correct classification probability against SNR for MIMO sonar systems with 10, 20, 50, 100, and 500 independent observations.

have been computed for MIMO sonar systems whose independent observations vary from 2 to 1000. Note that these simulations have been run with a 10-dB signal-to-noise ratio (SNR). Fig. 4(a) draws the probability of correct classification for each class depending on the number of observations. The first remark we can make is that it is possible to estimate the number of scattering points in a target if the number of scatterers is low (≤ 4). The two scattering point target can be seen as a dipole and its reflectivity pdf differs considerably from any n scattering point target (with $n \geq 2$). For this reason, fewer independent observations are needed to correctly classify this class of target. With only ten observations, a two scattering point target is correctly classified in 96% of cases. Table I provides the overall classification using our pdf matching algorithm depending on the number of independent observations. Only 100 independent observations are needed to reach an overall 92% correct classification.

In the second set of experiments, we computed the automatic target recognition (ATR) performance against noise. The MIMO observations were corrupted by an independent additive Rayleigh noise with an SNR varying from -10 to 20 dB. Fig. 4(b) displays the probability of correct classification using the conditional probability maximization from (20) against

TABLE I
OVERALL CORRECT CLASSIFICATION DEPENDING ON THE NUMBER OF OBSERVATIONS

number of observations	correct classification
10	64%
50	86%
100	92%
200	97%
500	99.81%
1000	>99.999999 %

the SNR level for MIMO systems with 10, 20, 50, 100, and 500 independent observations. The Bayesian classifier is based on matching target amplitude level to given pdfs. So it is not surprising that a certain SNR level is needed. In Fig. 4(b), the probability of correct classification stabilized at around 10-dB SNR. The surprising factor came from the fact that the classifier starts to perform better than random (25% correct classification) at a negative SNR (around -3 dB). With 500 observations and 0-dB SNR, the classifier reaches 70% of correct classification.

The ATR performances of spatially distributed MIMO systems came from the multiplicity of observations in a single snapshot. As long as the observations are statistically independent, such systems can provide meaningful statistical information about the target such as its pdf. We showed in this section an example of how to use this information to classify target based on its number of scatterers. Note that the important factor in the MIMO recognition capability is the independence of the observations. We develop and quantify this assumption in Section IV-C.

B. The Detection Problem With Statistical MIMO

The usual approach to the detection problem consists in evaluating the presence of a target of interest in the received signal $\mathbf{r}$. Under the null hypothesis $\mathcal{H}_0$, the received signal $\mathbf{r}$ contains only the noise $\mathbf{n}$. Under the target presence hypothesis $\mathcal{H}_1$, the received signal contains both the target signal and the noise. A detection rule function $\mathcal{F}(\mathbf{r})$ is compared to a given threshold η. If $\mathcal{F}(\mathbf{r}) < \eta$, the hypothesis $\mathcal{H}_0$ is chosen; if $\mathcal{F}(\mathbf{r}) \geq \eta$, the hypothesis $\mathcal{H}_1$ is chosen. We can distinguish two kinds of errors:

1) the false alarm: the detector detects a target ($\mathcal{F}(\mathbf{r}) \geq \eta$) when no target is present;
2) the missed detection: the detector misses a target ($\mathcal{F}(\mathbf{r}) < \eta$) when a target is present.

In the rest of this section, we compute the detection rule function $\mathcal{F}(\mathbf{r})$ under the hypothesis made in Section II.

Let $r_l(t)$ be the total received signal at the receiver l. According to our previous notations we have

$$r_l(t) = \sum_{k=1}^{K} z_{lk}(t) \tag{21}$$

where $z_{lk}(t)$ has been defined in (5). Let $\mathbf{x}$ be the $KL \times 1$ output vector from the filter bank $s_k^*(t)$ with $k \in [1, K]$. Note that $\mathbf{x}$ represents the match-filtered response and is computed as follows:

$$[\mathbf{x}]_{(l-1)L+k} = r_l \star s_k^*(t). \tag{22}$$

We assume that all the emitted pulses $s_k(t)$ are orthogonal so

$$s_i \star s_j^*(t) = \delta(i-j) \tag{23}$$

where δ denotes the discrete Dirac delta function. Note that MIMO waveform design for radar is still a very active part of research. If in practice purely orthogonal waveforms do not exist, different approaches are developed to minimize the waveform cross correlation including time, frequency, or code divided approaches. However, the study of orthogonal waveforms is beyond the scope of this paper and the reader can refer to [34]–[37] for more information on the subject.

Using (23) into (22), we arrive at

$$\begin{aligned}[\mathbf{x}]_{(l-1)L+k} &= r_l \star s_k^*(t) = \sum_{k=1}^{K} z_{lk} \star s_k^*(t) \\ &= z_{lk} \star s_k^*(t) = \sum_{q=1}^{Q} h_{lk}^{(q)}. \end{aligned} \tag{24}$$

We choose the following detection rule:

$$\mathcal{F}(\mathbf{r}) = \frac{1}{N}||\mathbf{x}||^2 = \frac{1}{N}\sum_{l,k}||x_{lk}||^2 \tag{25}$$

where $N = K \times L$ represents the total number of observations provided by the MIMO system. Using the same probability distribution stated in the model presented in Section IV-A, we deduce that under the $\mathcal{H}_1$ hypothesis, $\mathcal{F}(\mathbf{r})$ has the following probability distribution:

$$\mathcal{F}(\mathbf{r}) \sim \frac{1}{N}\sum_{n=1}^{N} \text{Rayleigh}^2(\sigma). \tag{26}$$

Using the properties of the Rayleigh distribution, we can write

$$\sum_{n=1}^{N} \text{Rayleigh}^2(\sigma) \sim \Gamma(N, 2\sigma^2) \tag{27}$$

where Γ is the Gamma distribution. So the pdf of the detection rule $\mathcal{F}(\mathbf{r})$ is $N.\Gamma(Nx, N, 1)$. The asymptotic behavior of the detection rule $\mathcal{F}(\mathbf{r})$ can be deduced from the following identity:

$$\lim_{N\to+\infty} N.\Gamma(Nx, N, 1) = \delta(1-x). \tag{28}$$

The convergence of the detection rule $\mathcal{F}(\mathbf{r})$ is shown in Fig. 5.

The proof of (28) is given in the Appendix. Equation (28) has interesting consequences: as the total number of observations N offered by the MIMO system increases, the pdf of the detection rule $\mathcal{F}(\mathbf{r})$ under the $\mathcal{H}_1$ hypothesis tends to the Dirac function δ_1. As a consequence, the random variable $\mathcal{F}(\mathbf{r})$ representing the target intensity averaged over all the MIMO observations collapses to a real number: the average RCS defined in Section II-A.

Haimovich [3] defines the average RCS as $E[\Sigma\Sigma^T] = 1$. This definition implies that the contribution of all the scatterers sums incoherently. Considering a target contained within a single resolution cell and assuming coherent sensors such as radar or sonar, the scattering points interact coherently with each other from a signal point of view. The random summation creates constructive and destructive interferences as explained with the random walk analogy in Section IV-A. We can then define the effective RCS as the effective average reflectivity of the target viewed by the sensors. We also demonstrated that we can very accurately model the effective RCS of a target with more than five scatterers by

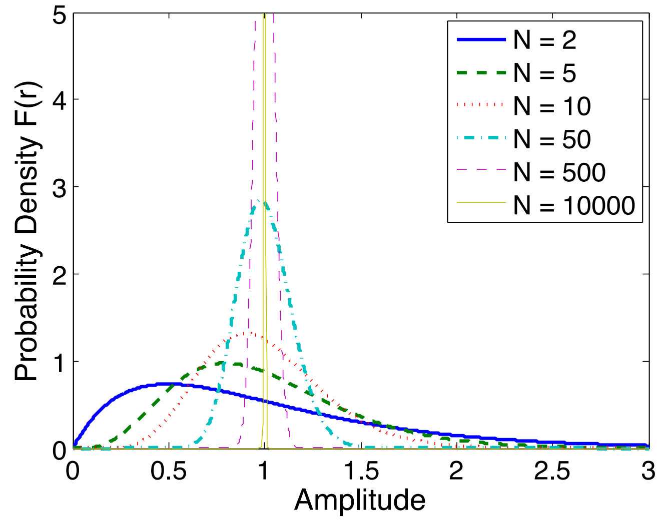

Fig. 5. Probability density function of $N.\Gamma(Nx, N, 1)$ for several values of N.

$$E\left[\text{Rayleigh}(\sigma)\right] = \sigma\sqrt{\frac{\pi}{2}} \tag{29}$$

where $\sigma = 1/\sqrt{2}$. So the effective RCS of the target is in fact

$$E[\{X_q\}] = \sqrt{\pi}/2. \tag{30}$$

It is important to note that $E[\{X_q\}] < 1$.

For this precise reason, the result given by (28) appears counterintuitive. We would have expected the detection rule function $\mathcal{F}(\mathbf{r})$ to tend to the mean of this Rayleigh distribution, i.e., $\sqrt{\pi}/2$, which represents the effective RCS defined earlier. The asymptotic behavior of $\mathcal{F}(\mathbf{r})$ gives a new insight into the capabilities of MIMO systems. It demonstrates indeed that as the number of independent observations increases, the MIMO detection system decorrelates the contribution of each scatterer in the echo signal and, in fact, solves the speckle noise in the target response. Fig. 5 shows the convergence speed of (28). Note that the convergence is relatively slow [especially when compared to the convergence speed of (16)]. This figure seems to indicate that roughly 100 observations are necessary to decorrelate scatterers within one-pixel resolution.

C. Super-Resolution Capabilities of Coherent MIMO Systems

In the previous section, we derived an important result: with a sufficient number of independent observations, MIMO systems can decorrelate the scatterer contributions within one-pixel resolution. It is in that sense that we understand the notion of "super-resolution": all the scatterers within one resolution cell decorrelate from each other. In other words, no artefacts induced by the imaging of one scatterer (e.g., sidelobes) will disrupt the imaging of the other scatterers. Super-resolution can then be achieved using MIMO systems under certain conditions. So far

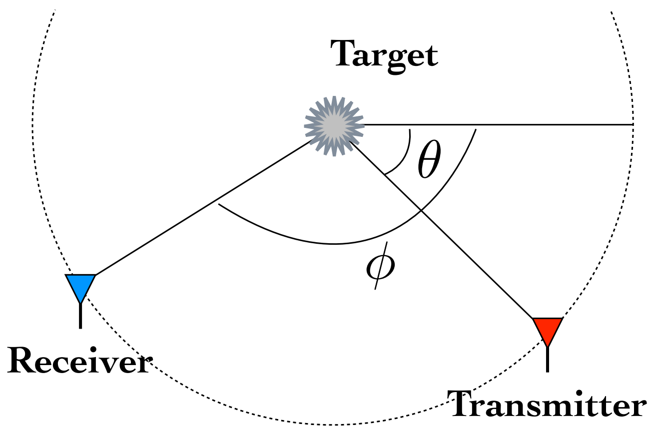

Fig. 6. Bistatic configuration. θ represents the view angle of the transmitter and ϕ represents the view angle of the receiver.

we have not taken into account the geometry of the target. We can reasonably assume that a target has a fixed geometry during the MIMO inspection. In this section, we intend to recover the target geometry via imaging. In Sections IV-A and IV-B, we analyzed the MIMO signals as statistical data. As the aim is now to image the target, we need to introduce the geometry of the MIMO sonar systems within its environment (i.e., the Tx and Rx locations). An observation is then linked to a particular configuration in the space, and each MIMO pair provides a view of the target. We then define independent views as follows.

Two views are independent if and only if their respective observations of a scene are statistically independent.

With the insight of the previous results we know that to achieve super-resolution the following conditions must be respected:

1) independent views: the antennas have to be sufficiently spaced to ensure the independence of each view;
2) decorrelation: the total number of views has to be large enough to ensure the scatterers decorrelation;
3) broadband: to achieve the range resolution needed, the MIMO system has to use broadband pulses for range compression.

So far we have assumed that all the MIMO observations were independent. This hypothesis was necessary for MIMO systems to achieve the recognition capability presented in Section IV-A and to solve the target speckle (cf., the Appendix). We stipulated that the antennas have to be sufficiently separated to ensure the independent view assumption. In the next paragraphs, we quantify the separation required to ensure independence and develop independence measure for MIMO systems depending on its geometry.

By introducing the term "view," we implicitly introduce the geometry and the configuration of the MIMO system. Let θ be the view angle of the transmitter and ϕ the view of the receiver. The bistatic configuration of a transmitter/receiver pair of the full MIMO system is drawn in Fig. 6 and will be noted (θ, ϕ). We are interested here in knowing the level of independence of a view $V(\theta_1, \phi_1)$ with another view $V(\theta_2, \phi_2)$. To measure the dependence of two random variables, the Pearson product–moment correlation coefficient or correlation coefficient is commonly used [38]. However, the correlation coefficient is not adequate here. First, this coefficient has been designed with a normal distribution assumption, and this assumption does not hold in our case. Second, this coefficient only measures linear correlation between the random variable. Finally, this coefficient is not a real independence measure in the sense that the correlation coefficient of two random variables can be null even if these random variables are dependent. To overcome this we propose to use the distance correlation introduced by Székely *et al.* [23]. Székely *et al.* define the distance covariance $\mathcal{V}$ as

$$\mathcal{V}^2 = \frac{1}{c_p c_q} \int_{\mathbb{R}_{p+q}} \frac{|f_{X,Y}(t,s) - f_X(t) f_Y(s)|^2}{|t|_p^{1+p} |s|_q^{1+q}} dtds \tag{31}$$

where f_X and $f_{X,Y}$ represent, respectively, the characteristic and the joined characteristic function of X or (X, Y); p and q are, respectively, the dimensions of the random vector X and Y; and c_d is defined as follows:

$$c_d = \frac{\pi^{(1+d)/2}}{\Gamma((1+d)/2)} \tag{32}$$

where $\Gamma(.)$ is the full gamma function. For $\mathcal{V}^2(X)\mathcal{V}^2(Y) \neq 0$, the distance correlation is then defined as

$$\mathcal{R}^2(X,Y) = \frac{\mathcal{V}^2(X,Y)}{\sqrt{\mathcal{V}^2(X)\mathcal{V}^2(Y)}}. \tag{33}$$

Székely *et al.* show [23] that $\mathcal{R}$ has "the properties of a true dependence measure" and, in particular, that two random vectors X and Y are independent if and only if $\mathcal{R}(X, Y) = 0$.

To assess the inter-views dependence of a MIMO system, 10^4 targets with two, three, four, or five scatterers were randomly generated. All the targets are contained in a cell of 3λ radius. Note that this MIMO system has a central frequency of $f_0 =$ 100 kHz and a bandwidth of $\Delta f = 40$ kHz. We will use this configuration for all the simulations within this section. For each target, its response V was computed as a function of the transmitter and receiver view angle (θ, ϕ). Each pair $(\theta, \phi), V(\theta, \phi)$ can then be considered as a random vector. The distance correlation $\mathcal{R}$ between all pairs $(\theta_n, \phi_n) \in [-\pi, \pi]^2$ is then computed. For the view angles (θ_0, ϕ_0), let $\mathcal{A}_0$ be the matrix defined by

$$\mathcal{A}_0(\theta, \phi) = \mathcal{R}(V(\theta_0, \phi_0), V(\theta, \phi)). \tag{34}$$

Note that in the point scatterer model there is a symmetry between the transmitter and the receiver and $V(\theta, \phi) = V(\phi, \theta)$. For this reason, the matrix $\mathcal{A}_0$ is symmetric along its first diagonal.

Let $\theta_1 = \theta_0 - \alpha$ and $\phi_1 = \phi_0 - \alpha$. Since the problem is axially symmetric, we can write that

$$\mathcal{A}_0(\phi, \theta) = \mathcal{A}_1(\phi - \alpha, \theta - \alpha). \tag{35}$$

So $\mathcal{A}_0(\theta, \phi)$ can be computed for only one θ_0. We chose $\theta_0 = 0$. For display purposes, we display in Fig. 7 the distance correlation matrix $1 - \mathcal{A}_0(\theta, \phi)$ for $\phi_0 = 0, \phi_0 = \pi/2$, and $\phi_0 = \pi$.

Fig. 7(a) displays the monostatic case; the transmitter and the receiver are in the same position: $\theta_0 = \phi_0 = 0$. Even though the monostatic configuration is convenient from a practical point of view it does not offer the best view in terms of correlation.

This article has been accepted for inclusion in a future issue of this journal. Content is final as presented, with the exception of pagination.

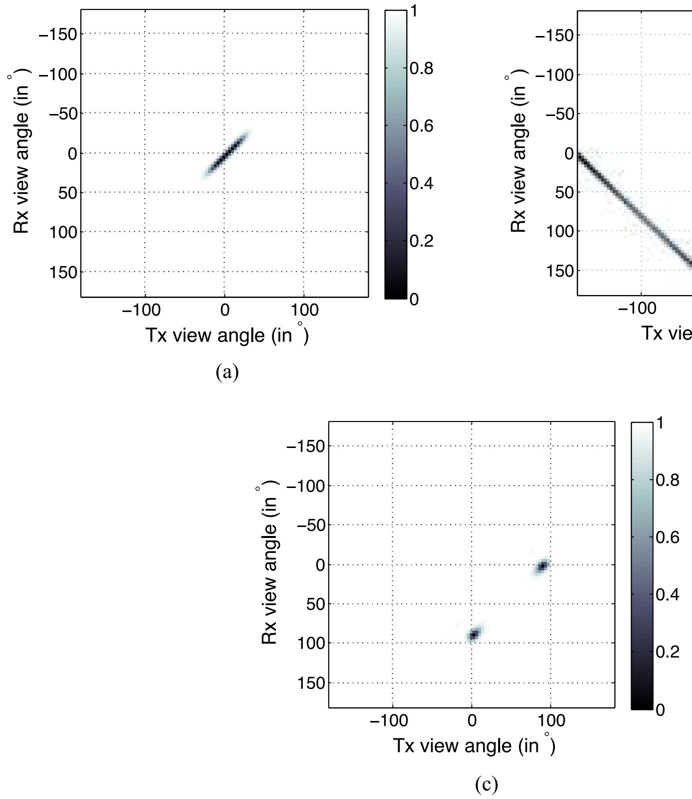

Fig. 7. Distance correlation matrix $1 - \mathcal{A}_0(\theta, \phi)$ for (a) $\phi_0 = 0$, (b) $\phi_0 = \pi$, and (c) $\phi_0 = \pi/2$.

The monostatic view correlates strongly with its neighbors ($\theta = +\alpha, \phi = -\alpha$) for $\alpha \in [-25^\circ, +25^\circ]$. It is interesting to note that the monostatic view correlates as well with ($\theta = \alpha, \phi = \alpha$) for $\alpha \in [-6^\circ, +6^\circ]$. So if we consider a monostatic sonar turning around the target for a full 360°, an average of 30 independent views will be obtained which is insufficient to achieve super-resolution.

In Fig. 7(b), the target is in-between the transmitter and the receiver. Although this configuration is not practical as the transmitted wave will arrive at the same time as the target echo to the receiver, it is interesting to note that all the opposite views $(\theta, \theta + \pi)$ for all θ correlate strongly.

Fig. 7(c) displays the distance correlation matrix with $\phi_0 = \pi/2$. As predicted, we observe a symmetry along the first diagonal and $\mathcal{A}_0(\theta, \phi) = \mathcal{A}_0(\phi, \theta)$. The correlation peaks are focused on (θ_0, ϕ_0) and (ϕ_0, θ_0). This configuration is the most effective as far as its independence is concerned, and the independence of this view toward its neighbors is maximized.

It is important to note that these results are dependent on the frequency used and the size of the cell. It can be shown that increasing the frequency and/or the cell narrows the peaks of Fig. 7(c). The potential number of independent views will then increase. However, the derivation of this result goes beyond the scope of this paper.

In the following simulation, we aim to demonstrate that we can recover the geometry of a target (i.e., the location of its scatterers). Given the results presented in Fig. 7 we chose

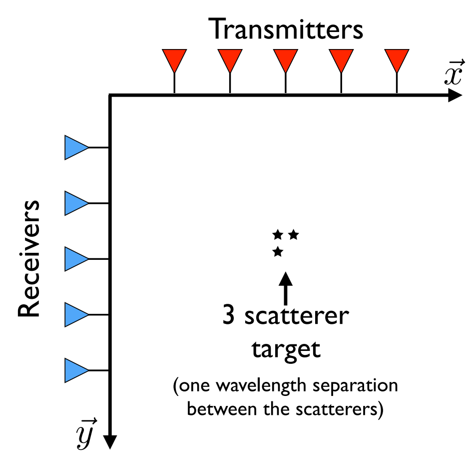

Fig. 8. MIMO configuration.

an "L" shape MIMO configuration as pictured in Fig. 8. The transmitters are placed along the x-axis, and the receivers are on the y-axis. For this experiment, the transducers are placed at an equal spacing along the axis. The number of transmitters and receivers and the spacing between them is adjustable. The central frequency of the MIMO sonar system is 100 kHz with a frequency band of around 40 kHz. We consider a three-point scatterer target centered at the point ($x = 20$ m, $y = 20$ m); the

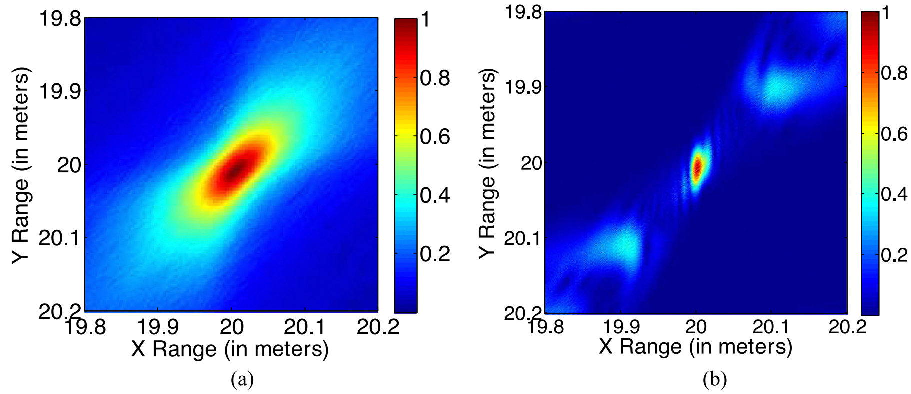

Fig. 9. Three-scatterer target MIMO image using: (a) 10 Tx, 10 Rx with incoherent processing; and (b) SIMO with 1 Tx and 10 Rx with 3-m spacing.

scatterers are separated by one wavelength which corresponds to 1.5 cm. Each scatterer has a reflectivity of $1/\sqrt{3}$.

To image the output of the MIMO system, we will use the multistatic backprojection algorithm which is a variant of the bistatic backprojection algorithm developed by the SAR community. Further details can be found in [39]–[41]. Using the backprojection algorithm, the SAS image is computed by integrating the echo signal along a parabola. In the bistatic case, the integration is done along ellipses. For the multistatic scenario, the continuous integration is replaced by a finite sum in which each term corresponds to one transmitter/receiver pair contribution. It is worth mentioning that, due to its sparse geometry, the MIMO imagery processing, using traditional backprojection techniques, will potentially develop grating lobes, which can be significant if the spatial sampling is regular. This problem is included in the more general imagery problem, or how to form a MIMO image. The subject is extremely vast and beyond the scope of this paper.

In Fig. 9(a), the MIMO image using incoherent processing is reconstructed (i.e., only the amplitude of the echoes has been used in the multistatic backpropagation algorithm). This figure represents in essence how the MIMO signal has been treated so far: the detection processing has been done using only the amplitudes of the different views. As expected, the three-scatterer target is represented only as a blob of energy. Note that the dimensions of this patch of energy represent the resolution limit of the incoherent system, which is approximately 10 cm $\times$ 10 cm.

For comparison purposes, we plot in Fig. 9(b) the target image obtained using a SIMO system with the same receiver array of ten receivers with 3-m spacing but only one transmitter. With only ten independent views, the scatterers within the target are unresolved and only a blob of energy is visible.

In Fig. 10(a), we have considered a MIMO system with ten transmitters and ten receivers with a spacing of 20 cm. For this scenario the 20-cm spacing breaks the widely spaced antenna assumption and the views are not exactly independent from each other. For this reason, we only observe a blob of energy at the target location.

In Fig. 10(c), the MIMO system consists of three transmitters and three receivers with 3-m spacing. In this case, the spacing between the antennas is several hundreds of wavelengths so the independence of the views is respected. However, the total number of views is $3 \times 3 = 9$ independent views which is relatively low according to the convergence speed of (28). In this scenario, the number of views is too low to ensure the decorrelation of the scatterers within the target. For this reason, only a blob of energy marks the target location. However, by closely inspecting the central blob, it is possible to distinguish a structure.

Finally, in Fig. 10(e), we consider a MIMO system with ten transmitters and ten receivers with a spacing of 3 m. With this configuration, we respect the conditions stipulated earlier and we are able to clearly image the three-scatterer target and in doing so achieve super-resolution imaging.

It is interesting to compare these results to the intra-views correlation of the different MIMO systems. Let us note $\{(\theta_n, \phi_n)_{n\in[1,N]}\}$ the views of the MIMO system. The level of intercorrelation for the full MIMO can be computed as

$$\mathcal{B}(\theta,\phi) = \max_{n\in[1,N]} \mathcal{A}_n(\theta,\phi). \tag{36}$$

In Fig. 10(b), (d), and (f) , we plot the $1-\mathcal{B}(\theta,\phi)$ functions for the same MIMO configurations as the ones explained in Fig. 10(a), (c) and (e), respectively. In Fig. 10(b), we are considering the 10×10 MIMO system with 20-cm separation between antennas. The 100 views produced by this configuration are all concentrated around the $(0^\circ, -90^\circ)$ view and are clearly all correlated to each other. The independent views assumption breaks down. In Fig. 10(d), the 3×3 MIMO configuration is considered. The 3-m spacing between the antenna ensures view independence and we can clearly see in the cluster nine peaks corresponding to each view. In Fig. 10(f), the 10×10 MIMO configuration is considered. Again, the 3-m antenna separation provides the necessary independence between the views and the 100 correlation peaks are visible and distinct from each other. The $\mathcal{B}(\theta,\phi)$ intercorrelation distance matrix then gives us an insight on how to design an efficient MIMO system and ensure the views independence. Assuming that the MIMO system provides enough views for recognition or super-resolution, each view (θ_n,ϕ_n) in $\mathcal{B}(\theta,\phi)$ should decorrelate as much as possible with the other views $(\theta_m,\phi_m)_{m\neq n}$.

In the second simulation, we aim to evaluate the distance resolution of the 10×10 MIMO system with 3-m spacing, as

This article has been accepted for inclusion in a future issue of this journal. Content is final as presented, with the exception of pagination.

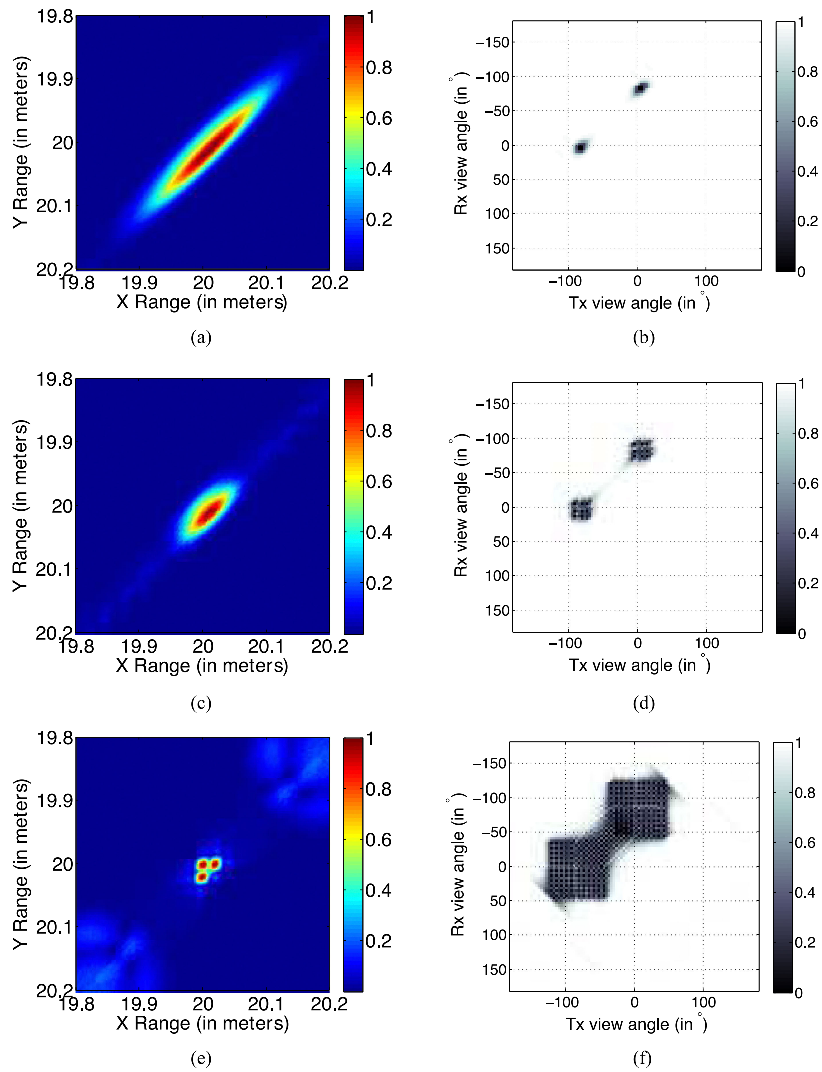

Fig. 10. MIMO target image given and full MIMO intercorrelation distance matrix $1 - \mathcal{B}(\theta, \phi)$ of (a) and (b) 10 Tx and 10 Rx with 20-cm spacing; (c) and (d) 3 Tx and 3 Rx with 3-m spacing; and (e) and (f) 10 Tx and 10 Rx with 3-m spacing.

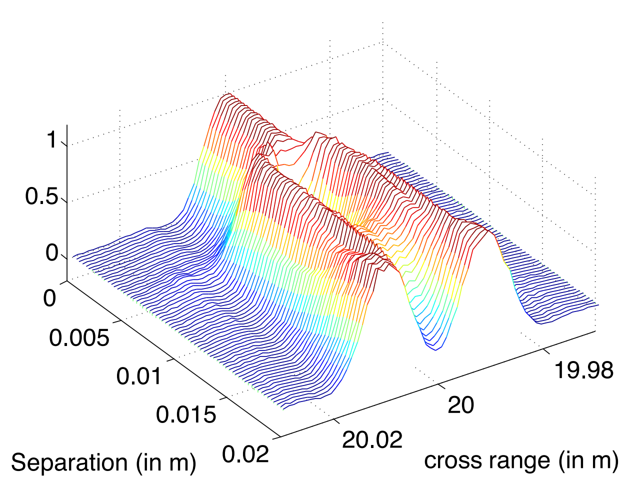

Fig. 11. Waterfall plot of the cross section of the two-scatterer MIMO image for a distance separation between 0 and 20 mm.

described in Fig. 10(e), by imaging two scatterers at 20-m range and separated by a distance d. Fig. 11 provides a waterfall plot of the cross section of the two-scatterer MIMO image for a distance separation between 0 and 20 mm. The MIMO system is able to separate two scatterers separated by 6 mm. To put this number into perspective, it is interesting to compute the maximum range resolution $c/2\Delta f$ where c is the speed of sound in water and Δf is the bandwidth of the pulse. In our case, the resolution in range is then around 2 cm. For the resolution in cross range, the theory predicts a resolution of $(k_{\max} - k_{\min})/c$. Here, we have $f_{\min} = 80$ kHz and $f_{\max} = 120$ kHz, which results in a resolution of around 3.75 cm. Equation (28) predicts statistically the super-resolution capability of MIMO systems. With this simulation, we show that large MIMO systems can achieve at least 3.5 times better resolution than other traditional systems.

For comparison purposes, we have computed the SAS image of the same target as described in Fig. 8 using the same frequency band and at the same range as in the previous experiment. The SAS image of the target is displayed in Fig. 12.

The SAS system runs in a straight line along the y-axis at 20-m range from the target. Using the phase center approximation, the SAS is seen as a single-channel system and the target

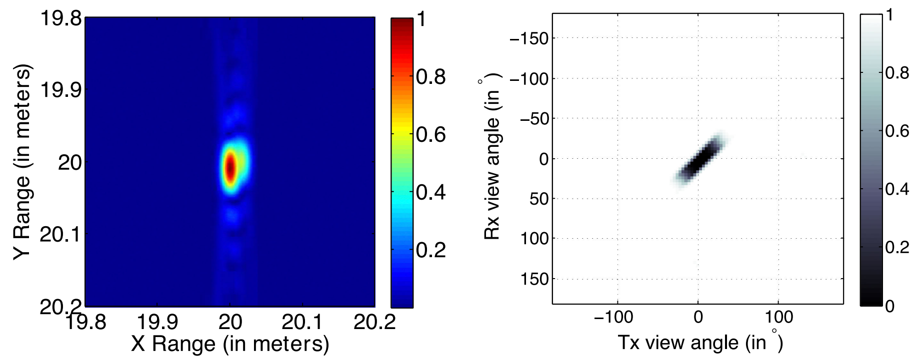

(a) (b)

Fig. 12. Three-scatterer target using SAS system. (a) SAS image. (b) $1 - \mathcal{B}(\theta, \phi)$ function for the SAS configuration.

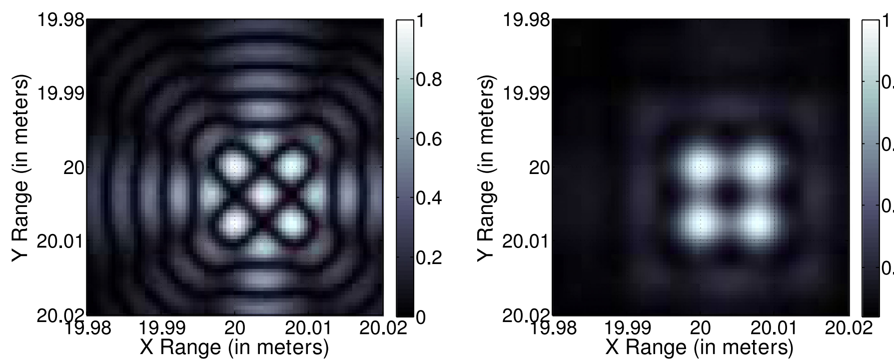

(a) (b)

Fig. 13. Four-scatterer target imaged with (a) circular SAS, and (b) 40×40 MIMO system.

echoes are computed at every $\lambda/2$ along the synthetic antenna. In Fig. 12(a), the beamwidth is fixed to $10°$. Note that the choice of a $10°$ beamwidth for this simulation was inspired by the $7°$ beamwidth of the MUSCLE SAS system from CMRE. In total, 467 echoes are computed and the SAS image is formed using backpropagation algorithm. Despite the high number of views and because all the SAS subviews are highly correlated, as shown in Fig. 12(b), the SAS system fails to separate the three scatterers. Using the same model and parameters as described in Section IV-C, we can infer that monostatic systems correlate on average for $12°$. With a $10°$ beamwidth, a SAS system then sees at most two to three independent views of the target. Note that in this aspect the SAS image reconstruction is based on the hypothesis that each pixel contains one scatterer. SAS systems require strong correlation between consecutive views to track and correct the echoes phase changes. So in that aspect, it is not surprising that the monoviews from SAS systems are so strongly correlated with each other.

Of course, the SAS system used in the previous experiment has a much smaller aperture than the 10×10 MIMO system described earlier. For the next experiment, we consider four scatterers target. Each scatterer is located at a vertex of a square whose size is $\lambda/2$. For the SAS system, we consider a circular SAS target acquisition at 20-m range from the target. For the MIMO system, we consider a 40×40 MIMO system. We call the element a collocated transmitter and receiver. Ten elements with 3-m spacing are placed on the axis $x = 0$ m, ten on the $y = 0$ m axis, ten on the $x = 40$ m line, and finally, ten on the $y = 40$ m line.

In that case, the $360°$ SAS aperture provides a total of 16756 echoes. These echoes are processed using a backprojection algorithm modified for the circular acquisition to form the image pictured in Fig. 13(a). Despite the maximum aperture of the SAS, the sidelobes induced by the proximity of the scatterers greatly deteriorate the image. The four scatterers are visible but barely distinguishable from their sidelobes. One can count five or even nine potential scatterers. Fig. 13(b) shows the MIMO image of the target. The target is resolved and the four scatterers are clearly separated. We estimated that the circular aperture of the SAS system provides approximately 35 independent views of the target. The 16756 SAS echoes are not statistically sufficient to fully resolve this specific target. However, the MIMO structure described above provides around 1300 independent views, which is enough to resolve the target. By carefully designing the MIMO system, we were able to provide enough independent views for the target to be properly imaged. In this instance, MIMO provides better imagery and more resolution than the SAS system.

V. Conclusion

In this paper, we have studied the fundamental principles of MIMO sonar systems. We have proposed a new formulation for broadband MIMO sonar systems by separating clearly the terms of propagation and the terms of target reflection. This formulation is more flexible than the one proposed by the radar community for different target model integration. The main advantage of statistical MIMO systems is to procure in a single snapshot a large number of independent views of a target of interest. The multiple independent observations can provide useful statistics of the target such as its pdf for example. We showed in this paper an example of how to use the MIMO signal and developed an algorithm to determine the number of scatterers contained in a target and then demonstrated the recognition capability of MIMO systems. Finally, we have explained why well-designed MIMO systems can achieve super-resolution and in certain cases surpass the resolution of SAS systems. By highlighting the fact that it is the independence between the views that makes MIMO sonar systems attractive, we provided guidelines to how and where the transmitters and the receivers should be placed. The MIMO sonar capabilities described in this paper make such a system a very attractive tool for surveillance. In a fixed environment, such as a harbor or a narrow channel, the transmitters and receivers elements can be carefully placed to ensure coverage and view independence. The recognition capabilities of MIMO sonar can then be used be identify threats.

Appendix
Proof of the Convergence of (28)

We demonstrate here the result given by (28). We stipulated that

$$\lim_{N\to+\infty} N.\Gamma(Nx, N, 1) = \delta(1-x) \tag{37}$$

where $\Gamma(x,k,\theta)$ represents the Gamma distribution function and $\delta(x)$ is the Dirac function. The Gamma distribution function is defined as follows:

$$\Gamma(x,k,\theta) = x^{k-1}\frac{\mathrm{e}^{-x/\theta}}{\theta^k\Gamma(k)} \tag{38}$$

with $x \geq 0$ and $k, \theta > 0$, and $\Gamma(k)$ represents the Gamma function. Note that $\Gamma(x,k,\theta) > 0$. In our case, we are looking at the convergence of

$$\begin{aligned} N.\Gamma(Nx,N,1) &= N(Nx)^{N-1}\frac{\mathrm{e}^{-Nx}}{\Gamma(N)} \\ &= \frac{N^N}{\Gamma(N)\mathrm{e}^N}.\frac{\left(x\mathrm{e}^{1-x}\right)^N}{x} \\ &= A(N)f(x,N) \end{aligned} \tag{39}$$

where $A(N) = N^N/\Gamma(N)\mathrm{e}^N$ and $f(x,N) = (x\mathrm{e}^{1-x})^N/x$. Note that $A(N)$ represents a normalization factor and for all N

$$\int_{x=0}^{+\infty} x^{N-1}\mathrm{e}^{N(1-x)}dx = \frac{1}{A(N)}. \tag{40}$$

Asymptotic Behavior of $A(N)$: To get the asymptotic behavior of $A(N)$, we use the Stirling formula

$$n! \sim \sqrt{2\pi n}\left(\frac{n}{\mathrm{e}}\right)^n \tag{41}$$

$$\begin{aligned} A(N) &= \frac{N^N}{\Gamma(N)\mathrm{e}^N} \\ &\sim \frac{\mathrm{e}^{N-1}}{\sqrt{2\pi(N-1)}(N-1)^{N-1}}\frac{N^N}{\mathrm{e}^N} \\ &\sim \left(\frac{N}{N-1}\right)^{N-1}\frac{1}{\mathrm{e}}\frac{N}{\sqrt{2\pi(N-1)}} \\ &\sim \left(\frac{N}{N-1}\right)^{N-1}\frac{1}{\mathrm{e}}\sqrt{\frac{N}{2\pi}}. \end{aligned} \tag{42}$$

By using the following identity:

$$\lim_{n\to+\infty}\left(\frac{n}{n-1}\right)^{n-1} = \mathrm{e} \tag{43}$$

we arrive at

$$A(N) \sim \sqrt{\frac{N}{2\pi}}. \tag{44}$$

It is important to note that $\lim_{N\to+\infty} A(N) = +\infty$.

Study of the $f(x,N)$ Function: The $f(x,N)$ function has the following properties:

$$f(x,N) > 0, \quad \text{for all } x, N \geq 0 \tag{45}$$

$$f(0,N) = 0, \quad \text{for } N > 0 \tag{46}$$

$$\lim_{x\to+\infty} f(x,N) = 0 \tag{47}$$

$$f(x,N) \leq f(x_N,N), \quad \text{where } x_N = 1 - \frac{1}{N} \tag{48}$$

$$f(x_N,N) = \left(\frac{N-1}{N}\right)^{N-1}\mathrm{e} \to 1, \quad \text{when } N \to +\infty \tag{49}$$

$$f(x,N+1) \leq f(x,N). \tag{50}$$

It is also important to note that $f(x,N)$ is an increasing function from 0 to x_N and a decreasing function from x_N to $+\infty$.

Convergence of the $A(N)f(x,N)$ Function: To prove that the $A(N)f(x,N)$ function converges to a Dirac function, we need to demonstrate the following properties:

$$\lim_{N\to+\infty}\int_{x=0}^{+\infty} A(N)f(x,N)dx = 1 \tag{51}$$

$$\lim_{N\to+\infty} A(N)f(x,N) = 0, \text{ for } x \neq 1 \tag{52}$$

$$\lim_{N\to+\infty} A(N)f(1,N) = +\infty. \tag{53}$$

Property (51) is given by definition: $A(N)f(x,N)$ represents a probability density so for all N we have $\int_{x=0}^{+\infty} A(N) f(x,N)dx = 1$.

Proof of (53): For $x = 1$, we have

$$\lim_{N\to+\infty} A(N)f(1,N) = \lim_{N\to+\infty} A(N) \times \lim_{N\to+\infty} f(x_N, N) = \lim_{N\to+\infty} A(N) = +\infty. \tag{54}$$

Proof of (52): For $x \neq 1$, we want to prove that $\lim_{N\to+\infty} A(N)f(x,N) = 0$. To demonstrate this, we need to proceed using *reductio ad absurdum*.

We suppose that there exists an $x_0 \neq 1$, a $\xi > 0$, and a $N_0 \geq 0$ such that for all $N \geq N_0$, $f(x_0, N) > \xi$. We suppose here that $x_0 < 1$. Note that the proof for $x_0 > 1$ is identical and is left to the reader. We can choose N_0 such that $N_0 > 1/1 - x_0$. Note that $\eta = 1 - x_0/2$

$$\begin{aligned}\int_{x=0}^{+\infty} A(N)f(x,N)dx &\geq \int_{x=x_0}^{1-\frac{1}{N}} A(N)f(x,N)dx \\ &\geq A(N)\left(1 - \frac{1}{N} - x_0\right) \\ &\quad \times \min_{x\in[x_0,1-\frac{1}{N}]} (f(x,N)) \\ &\geq A(N)\cdot\eta\cdot\xi \end{aligned} \tag{55}$$

So

$$\begin{aligned} A(N)\eta\xi &\leq 1 \\ \xi &\leq \frac{1}{\eta A(N)}, \text{ for all } N > N_0. \end{aligned} \tag{56}$$

We deduce from the last equation that $\lim_{N\to\infty} A(N) = +\infty$, $\xi = 0$ which is in contradiction with the hypothesis.

So for all $x \neq 1$, $\lim_{N\to\infty} A(N)f(x,N) = 0$ ∎

REFERENCES

[1] H. D. Griffiths, C. J. Baker, P. F. Sammartino, and M. Rangaswamy, *MIMO as a Distributed Radar System*, New York, NY, USA: Wiley, 2008, Ch. 8, pp. 319–363. [Online]. Available: http://dx.doi.org/10.1002/9780470391488.ch8.

[2] J. Li and P. Stoica, "MIMO radar with colocated antennas," *IEEE Signal Process. Mag.*, vol. 24, no. 5, pp. 106–114, Sep. 2007.

[3] A. Haimovich, R. Blum, and L. Cimini, "MIMO radar with widely separated antennas," *IEEE Signal Process. Mag.*, vol. 25, no. 1, pp. 116–129, 2008.

[4] D. Bliss and K. Forsythe, "Multiple-input multiple-output (MIMO) radar and imaging: Degrees of freedom and resolution," in *Proc. 37th Asilomar Conf. Signals Syst. Comput.*, pp. 54–59, 2003, doi: 10.1109/ACSSC.2003.1291865.

[5] E. Fishler *et al.*, "MIMO radar: An idea whose time has come," in *Proc. IEEE Int. Conf. Radar*, 2004, DOI: 10.1109/NRC.2004.1316398.

[6] E. Fishler *et al.*, "Spatial diversity in radars-models and detection performance," *IEEE Trans. Signal Process.*, vol. 54, no. 3, pp. 823–838, Mar. 2006.

[7] D. Rabideau, "Ubiquitous MIMO digital array radar," in *Proc. 37th Asilomar Conf. Signals Syst. Comput.*, 2003, DOI: 10.1109/ACSSC.2003.1292087.

[8] C. Du, "Performance evaluation and waveform design for MIMO radar," Ph.D. dissertation, Edinburgh Univ., Edinburgh, U.K., 2010.

[9] N. Lehmann *et al.*, "Evaluation of transmit diversity in MIMO-radar direction finding," *IEEE Trans. Signal Process.*, vol. 55, no. 5, pp. 2215–2225, May 2007.

[10] C. Du, Y. Petillot, and J. Thompson, "Predicted detection performance of MIMO radar," *IEEE Signal Process. Lett.*, vol. 15, pp. 83–86, 2008.

[11] F. Robey, S. Coutts, D. Weikle, J. McHarg, and K. Cuomo, "MIMO radar theory and experimental results," in *Proc. 38th Asilomar Conf. Signals Syst. Comput.*, 2004, DOI: 10.1109/ACSSC.2004.1399141.

[12] I. Bekkerman and J. Tabrikian, "Target detection and localization using MIMO radars and sonars," *EEE Trans. Signal Process.*, vol. 54, pp. 3873–3883, 2006.

[13] N. Lehmann, A. Haimovich, R. Blum, and L. Cimini, "MIMO-radar application to moving target detection in homogenous clutter," in *Proc. Adaptive Sensor Array Process. Workshop*, 2006, p. 1.

[14] N. Lehmann, A. Haimovich, R. Blum, and L. Cimini, "High resolution capabilities of MIMO radar," in *Proc. 40th Asilomar Conf. Signals Syst. Comput.*, 2006, DOI: 10.1109/ACSSC.2006.356576.

[15] S. Kim, B. Ku, W. Hong, and H. Ko, "Performance comparison of target localization for active sonar systems," *IEEE Trans. Aerosp. Electron. Syst.*, vol. 44, no. 4, pp. 1371–1380, 2008.

[16] M. Fewell and S. Ozols, "Simple detection-performance analysis of multistatic sonar for anti-submarine warfare," *DSTO Defence Sci. Technol. Organisation, Tech. Rep.*, 2011.

[17] R. Been *et al.*, "Multistatic sonar: A road to a maritime network enabled capability," in *Undersea Defence Technol. Eur.*, Naples, Italy 2007.

[18] F. Ehlers, "Final report on deployable multistatic sonar systems," NATO Undersea Res. Cntr., Tech. Rep., 2009.

[19] S. Benen and P. Berkel, "Fusion concepts for multistatic sonar systems," in *INFORMATIK 2011—Informatik Schafft Communities*, 2011.

[20] M. Daun and F. Ehlers, "Tracking algorithms for multistatic sonar systems," *EURASIP J. Adv. Signal Process.*, 2010, DOI: 10.1155/2010/461538.

[21] D. Orlando and F. Ehlers, "Advances in multistatic sonar," *Sonar Syst.*. InTech, 2011, pp. 29–50.

[22] D. Grimmett, "Automatic identification of specular detections in multistatic sonar systems," in *Proc. MTS/IEEE OCEANS Conf. Biloxi—Marine Technology for Our Future: Global and Local Challenges*, 2009, pp. 1–10.

[23] G. J. Székely, M. L. Rizzo, and N. K. Bakirov, "Measuring and testing dependence by correlation of distances," *Ann. Stat.*, vol. 35, pp. 2769–2794, 2007.

[24] M. Skolnik, *Introduction to Radar Systems*, New York, NY, USA: McGraw-Hill, 2002, ch. 2, pp. 20–71.

[25] C. Capus *et al.*, "Bio-inspired wideband sonar signals based on observations of the bottlenose dolphin (tursiops truncatus)," *J. Acoust. Soc. Amer.*, vol. 121, no. 1, pp. 594–604, 2007.

[26] Y. Pailhas, C. Capus, K. Brown, and P. Moore, "Measured target responses to bio-inspired sonar pulses," in *Proc. 8th Eur. Conf. Underwater Acoust.*, 2006, pp. 109–114.

[27] R. Urick, *Principles of Underwater Sound*, New York, NY, USA: McGraw-Hill, 1975, ch. 2, pp. 17–30.

[28] Y. Pailhas, C. Capus, and K. Brown, "The multiview limitation of target classification by broadband echo analysis," in *Proc. IEEE OCEANS Eur. Conf.*, 2007, DOI: 10.1109/OCEANSE.2007.4302475.

[29] Y. Pailhas, C. Capus, K. Brown, and P. Moore, "Analysis and classification of broadband echoes using bio-inspired dolphin pulses," *J. Acoust. Soc. Amer.*, vol. 127, no. 6, pp. 3809–3820, 2010. [Online]. Available: http://link.aip.org/link/?JAS/127/3809/1.

[30] Y. Pailhas, C. Capus, and K. Brown, "Permanent scatterers detection using raw SAS data," in *Proc. Eur. Conf. Underwater Acoust.*, 2012, doi: 10.1121/1.4772726.

[31] W. R. Hamilton, "Theory of systems of rays," *Trans. Roy. Irish Acad.*, vol. 15, pp. 69–174, 1828.

[32] R. Doolittle and H. Uberall, "Sound scattering by elastic cylindrical shells," *J. Acoust. Soc. Amer.*, vol. 39, no. 2, pp. 272–275, 1966.

[33] A. C. Berry, "The accuracy of the Gaussian approximation to the sum of independent variates." *Trans. Amer. Math. Soc.*, vol. 49, pp. 122–136, 1941.

[34] D. J. Rabideau, "MIMO radar waveforms and cancellation ratio," *IEEE Trans. Aerosp. Electron. Syst.*, vol. 48, no. 2, pp. 1167–1178, Apr. 2012.

[35] H. Khan and D. Edwards, "Doppler problems in orthogonal MIMO radars," in *Proc. IEEE Conf. Radar*, Apr. 2006, DOI: 10.1109/RADAR.2006.1631806.

[36] G. V. K. Sharma and K. R. Rajeswari, "MIMO radar ambiguity optimization using phase coded pulse waveforms," *Int. J. Comput. Appl.*, vol. 61, no. 10, pp. 18–23, Jan. 2013.

[37] X. Song, S. Zhou, and P. Willett, "Reducing the waveform cross correlation of MIMO radar with space time coding," *IEEE Trans. Signal Process.*, vol. 58, no. 8, pp. 4213–4224, Aug. 2010.

[38] J. L. Rodgers and W. A. Nicewander, "Thirteen ways to look at the correlation coefficient," *Amer. Stat.*, vol. 42, no. 1, pp. 59–66, 1988.

[39] N. J. Willis, *Bistatic Radar*, Norwood, MA, USA:Artech House, 1991, ch. 5, pp. 85–118.
[40] A. Home and G. Yates, "Bistatic synthetic aperture radar," in *Proc. IEEE RADAR*, 2002, pp. 6–10.
[41] O. Arikan, "A tomographic formulation of bistatic synthetic aperture radar," in *Proc. ComCon*, 1988, pp. 289–302.

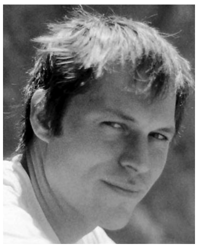

Yan Pailhas received the Ph.D. degree in sonar systems and underwater acoustics from Heriot-Watt University, Edinburgh, U.K., in 2012 and the M.Sc. degree in signal and image processing from the Ecole Nationale Supérieure de Cachan, Cachan, France, in 2003. He also received two Engineering degrees in telecommunications with a specialization in image and signal processing from the Ecole Nationale Supérieure des Télécommunications, Paris, France, and from the Politecnico di Torino, Torino, Italy.

He has been a Research Associate in the Ocean Systems Laboratory, Heriot-Watt University, since 2004, where he is currently carrying out research activities in bioacoustic signals and sensors, signal processing for detection and classification, and numerical simulations.

Yvan R. Petillot (M'03) received the engineering degree in telecommunications with a specialization in image and signal processing, the M.Sc. degree in optics and signal processing, and the Ph.D. degree in real-time pattern recognition using optical processors from the Universitée de Bretagne Occidentale, Ecole Nationale Supérieure des Télécommunications de Bretagne (ENSTBr), Brest, France.

He is a specialist in sonar data processing (including obstacle avoidance) and sensor fusion. He is currently a Professor at Heriot-Watt University, Edinburgh, U.K., where he leads the Sensor Processing Group of the Oceans Systems Laboratory, focusing on image interpretation and mine and counter measures.

Dr. Petillot is a reviewer of various IEEE TRANSACTIONS and a member of the IEEE.

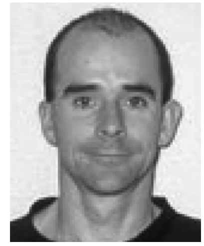

Keith Brown received the B.Sc. degree in electrical and electronic engineering and the Ph.D. degree on the application of knowledge-based techniques to telecoms equipment fault diagnosis from the University of Edinburgh, Edinburgh, Scotland, in 1984 and 1988, respectively.

He is currently a Senior Lecturer at Heriot-Watt University, Edinburgh, U.K., and part of the Edinburgh Research Partnership's Joint Research Institute for Signal & Image Processing. His research interests in bioinspired signal design and analysis and intelligent systems.

Bernard Mulgrew (F'12) received the B.Sc. degree from Queen's University Belfast, Belfast, Northern Ireland, in 1979 and the Ph.D. degree from the University of Edinburgh, Edinburgh, U.K., in 1987.

After his undergraduate studies, he worked for four years as a Development Engineer in the Radar Systems Department, Ferranti, Edinburgh, U.K. From 1983 to 1986, he was a Research Associate in the Department of Electrical Engineering, University of Edinburgh, Edinburgh, U.K. He was appointed to lectureship in 1986, promoted to Senior Lecturer in 1994, and became a Reader in 1996. The University of Edinburgh appointed him to a Personal Chair in October 1999 (Professor of Signals and Systems). He currently holds the Royal Academy of Engineering Chair in Signal Processing. His research interests are in adaptive signal processing and estimation theory and in their application to radar and sensor systems. He is a coauthor of three books on signal processing.